Acta Materialia 274 (2024) 120018

Contents lists available at ScienceDirect

Acta Materialia

journal homepage: www.elsevier.com/locate/actamat

Full length article

Genetic design of precipitation-hardening stainless steels for additive manufacturing

Hossein Eskandari Sabzi [a,b,*], Seoung-Ho Lim [c], Diego Della Crociata [d], Roger Castellote-Alvarez [e], Marco Simonelli [d], David San-Martín [e], Xinjiang Hao [a], Pyuck-Pa Choi [c], Pedro E.J. Rivera-Díaz-del-Castillo [b,**]

[a] Globus Metal Powders, Eston Road, Middlesbrough, TS6 6US, United Kingdom
[b] School of Engineering, University of Southampton, Highfield Campus, Southampton, SO17 1BJ, United Kingdom
[c] Department of Materials Science and Engineering, Korea Advanced Institute of Science and Technology (KAIST), 291 Daehak-ro, Yuseong-gu, Daejeon, 34141, Republic of Korea
[d] Centre for Additive Manufacturing, University of Nottingham, Nottingham, NG8 1BB, United Kingdom
[e] MATERALIA Group, Department of Physical Metallurgy, Centro Nacional de Investigaciones Metalurgicas (CENIM-CSIC), Av. Gregorio del Amo 8, Madrid, 28040, Spain

ARTICLE INFO

Keywords:
Precipitation hardening steels
Additive manufacturing
Laser powder bed fusion
Cu-rich precipitates
Atom probe tomography

ABSTRACT

A genetic algorithm for the design of precipitation-hardening (PH) stainless steels (SSs) for additive manufacturing (AM) is presented. A fully martensitic matrix is found to be the key factor for achieving the maximum strength but, unlike earlier studies, *in situ* ageing treatment unique to AM is also taken into consideration, leading to the promotion of precipitation of Cu-rich precipitates during AM. Design theories are integrated to a genetic algorithm optimisation framework to maximise strength and printability. Experimental proof of concept was made by fabricating the novel alloy components using laser powder bed fusion (LPBF) AM, and was compared to a commercial LPBFed 17-4 PH SS. The results are consistent with the goals of the design strategy. The superior mechanical properties of the designed alloy were attributed mainly to a combination of two factors: precipitation hardening and dislocation strengthening. Precipitation hardening, controlled by a high dislocation density of the matrix as a result of dislocation multiplication and annihilation during printing, is the main responsible for the improvement of yield strength of the LPBFed novel PH SS.

1. Introduction

Precipitation hardening is a mechanism to increase the strength and hardness of certain alloys such as steels, aluminium, and nickel alloys, without sacrificing toughness. Traditionally, the microstructure of precipitation-hardening stainless steels (PH SSs) consists of a martensitic matrix with a controlled amount of δ-ferrite and austenite [1,2]. The δ-ferrite phase, although beneficial for enhancing ductility and toughness, limits the achievable strength levels [3]. To further enhance the mechanical properties of PH SSs, researchers have sought innovative approaches to tailor its microstructure. One such approach involves alloy modification, with the incorporation of elements such as Cu and Nb that can profoundly impact the material's behaviour during solidification and subsequent heat treatment.

One effect of Cu addition is the precipitation of Cu-rich particles in the martensitic matrix, which primarily takes place after ageing heat treatment, strengthening the martensite [4,5]. Typically, the strengthening procedure involves quenching from austenite to generate a martensitic structure, followed by an ageing process to control precipitation [6]. Yield and ultimate tensile strength of PH SSs can be tailored by modifying parameters such as volume fraction and size of the precipitates [7]. Due to their strength, ductility, and corrosion resistance, these alloys are perfectly suited for applications in marine environments, power plants, chemical production, and aerospace industries [8]. However, due to their high hardness and tensile strength, casting methods may not be a suitable approach for their manufacturing, necessitating the use of wrought techniques to enhance their mechanical properties. Moreover, the high strength of such wrought products makes it challenging to machine them into intricate structural components.

Additive manufacturing (AM) is an effective method to fabricate PH SS components. Laser powder bed fusion (LPBF) has been adopted

* Corresponding author at: School of Engineering, University of Southampton, Highfield Campus, Southampton, SO17 1BJ, United Kingdom.
** Corresponding author.
E-mail addresses: h.eskandari-sabzi@soton.ac.uk (H.E. Sabzi), p.rivera@soton.ac.uk (P.E.J. Rivera-Díaz-del-Castillo).

https://doi.org/10.1016/j.actamat.2024.120018
Received 14 March 2024; Received in revised form 14 May 2024; Accepted 14 May 2024
Available online 23 May 2024

Table 1
Tensile mechanical properties of as-printed alloys (17-4 PH and 15-5 PH), as well as wrought alloys (17-4 W and 15-5 W). Yield strength (σ_Y), Tensile strength (TS), elongation (EL). The results of this study are also shown in this Table.

Alloy	Hardness (HV)	σ_Y (MPa)	TS (MPa)	El (%)	Ref.
17-4 PH	300–350	520	1150	8	[10]
17-4 PH	–	678	975	12	[18]
17-4 PH	362–380	734–944	–	19–20	[19]
17-4 PH	360	937	1008	8	[20]
17-4 PH	358–365	–	–	–	[11]
17-4 PH	–	830	887	–	[21]
17-4 W	424	1240	1340	10	[22]
15-5 PH	–	800–900	1100–1200	14–19	[23]
15-5 PH	348–378	563–726	1047–1105	9–13	[24]
15-5 PH	380	–	–	–	[25]
15-5 PH	–	980	–	9	[26]
15-5 PH	–	1000–1050	–	9	[27]
15-5 PH	338	–	–	–	[28]
15-5 PH	326	585	1085	20	[29]
15-5 PH	–	853	944	2	[30]
15-5 PH	–	758–846	–	–	[31]
15-5 W	424	1200	1340	15	[32]
This study	426 ± 16	1218 ± 68	1431 ± 5	10 ± 1	

to produce dense and relatively homogeneous 17-4 and 15-5 PH SS components [9–13]. Due to ultra-fast heating and cooling rates imposed during LPBF, the control of unique microstructures down to the nanoscale is feasible. However, the coarse and columnar grain structure, and the presence of retained austenite and δ-ferrite, that affect subsequent precipitation hardening and mechanical properties, are thought to be the main issues of LPBFed PH SSs [10,14–17]. Here we report an alloy design strategy to tailor microstructure and mechanical properties of PH SS components fabricated by LPBF. We demonstrate the possibility to modify chemical composition to achieve a fully martensitic microstructure, and that optimisation of processing parameters activates an *in situ* heat treatment upon printing; these are effective solutions to fabricate PH SS components with superior mechanical properties compared to their wrought counterparts. This strategy is distinct from the conventional alloy design strategies, which are mainly based on limited thermodynamic considerations.

Recent studies have revealed that, in the as-printed state, AMed 17-4 and 15-5 PH SSs exhibit lower tensile properties compared to their wrought counterparts (Table 1). Wrought condition in here refers to solution treated, quenched, and aged specimens. Based on Table 1, a wide range of tensile properties can be achieved through application of various AM process parameters and techniques. However, still solution treatment and ageing, or a direct ageing treatment, are essential to meet the industrial strength requirements of AMed PH SSs, which increase the manufacturing costs of such steels. A significant technological breakthrough would be achieved if AM would circumvent the need of post-heat treatment, whilst attaining better mechanical properties than wrought alloys; this is presented in this work.

To address these drawbacks and implement an efficient design strategy, theoretical and phenomenological models of microstructure evolution need to be taken into consideration. Genetic algorithms (GAs) are effective population-based robust search and optimisation techniques [33]. In order to find a global optimum, GAs apply Darwinian concepts of the survival of the fittest. In this study, the microstructural evolution and mechanical properties of GA-designed PH SS alloy components fabricated using LPBF was investigated. The addition of Cu and the resultant microstructural changes during LPBF are thoroughly investigated to elucidate their influence on the material's performance. Moreover, the mechanical properties of as-built GA-designed PH SS alloy are compared with those of conventional 17-4 PH SS and 15-5 PH SS. The objective of this research is to provide insights into the synergy between genetic alloy design, LPBF, and the resulting microstructural evolution in enhancing the mechanical properties of 17-4 PH SS.

Table 2
Search ranges of all alloying elements employed in this study for optimisation in wt.%.

	Cr	Ni	Cu	Nb	Mn	Si	C	N	Fe
Min	12	2	2	0.1	0.01	0.01	0.01	0.01	Bal.
Max	19	6	7	0.6	2	1	0.03	0.1	Bal.

2. Genetic modelling

The starting point is the alloy design process based on a GA. The GA provides an optimisation framework to maximise a quantitative feature. In this case, the precipitation hardening contribution to strengthening is maximised by alteration of the alloy chemical composition. The alloy system considered in the GA is based on the nominal composition of 17-4 PH SS, which consists of Fe, Cr, Ni, Cu, Mn, Si, Nb, C, and N, where the amounts of Fe are balanced. The concentration ranges employed for each element in the optimisation framework are listed in Table 2. This algorithm iteratively evaluates potential compositions against set performance metrics, which are mechanical strength, corrosion resistance, and printability. The whole computational alloy design model is implemented in a Matlab programme, which is linked to Thermo-Calc software using the TC-toolbox interface [34]. A lath martensite matrix with a homogeneous dispersion of fine precipitates can lead to a combination of high strength and good ductility. We aimed to achieve this microstructure upon printing rather than through a two-step heat treatment process that involves first treating the material at high temperatures to create a homogeneous, fully austenitic state, then quenching it to room temperature to create a martensitic matrix, and finally ageing it at a low temperature to allow desirable species to precipitate in the finely grained matrix structure, which is the common approach to AM 17-4 PH.

Different phases, such as various carbide species and δ-ferrite, can be present in the as-printed condition depending on the composition of the alloy. Since such phases typically have a negative impact on the mechanical properties, it is preferable to begin with a pure austenitic matrix upon solidification, then a totally martensitic structure can be achieved after the ultra-fast cooling of LPBF. By encouraging the formation of suitable precipitates, such as Cu precipitates and Nb carbides, with the appropriate dispersion of a dense network of nanosized particles, ageing treatment can also take place *in situ* (in the powder bed) to further reinforce the fully martensitic matrix. Furthermore, after promoting the precipitation, a suitable concentration of Cr in the matrix at the typical ageing temperature must be assured to provide adequate corrosion resistance. In addition to these, printability is promoted by minimising the solidification temperature range and maximising the performance index of the alloy [35].

A computational alloy design model combined with a genetic algorithm has been created in order to produce the intended microstructures mentioned above. The corresponding flow diagram is shown in Fig. 1. Every potential solution is assessed based on the go/no-go criteria. Each go/no-go requirement must be met in order for subsequent evaluations to continue:

1. Equilibrium solidification temperature range (STR), which is the difference between the liquidus and solidus temperature of the alloy, is determined through Thermo-Calc software (TCFE10 database) and imposed as the first go/no-go condition of STR being lower than 61 °C. This has been obtained based on previously LPBFed 17-4 PH SS compositions that were reported in the literature [10,14,16,36–45]. Those compositions and their corresponding STRs are listed in Table 3. This is to minimise formation of solidification cracks during LPBF.
2. Performance index (PI), which is the ratio between the yield strength (solid solution strengthening) and the coefficient of thermal expansion [35] being larger than 1.55×10^6 MPa.K. This is the second criterion to avoid hot cracks during LPBF.

Table 3
Chemical composition (in wt.%) of the reported LPBFed 17-4 PH SSs in the literature, with their corresponding STRs, calculated from Thermo-Calc.

Cr	Ni	Cu	Mn	Si	Nb	C	N	Fe	STR	Ref.
16.1	4.34	3.81	0.87	0.71	0.32	0.03	0.1	Bal.	61	[14]
15.84	4.55	3.87	0.32	0.36	0.37	0.019	0.01	Bal.	59	[36]
17.7	4.2	3.3	1	0.07	0.14	0.07	–	Bal.	70	[10]
15.6	4.03	3.89	0.24	0.29	0.33	0.01	–	Bal.	55	[10]
15.8	4.6	3.67	0.51	0.32	0.32	0.01	0.02	Bal.	56	[37]
16.39	4.78	3.57	0.66	0.03	0.21	0.03	–	Bal.	55	[38]
17.1	4.4	4.42	0.85	0.92	0.24	0.027	0.009	Bal.	60	[39]
16.66	4.51	4.32	0.52	0.41	0.35	0.037	–	Bal.	67	[40]
16.2	4.2	3.8	0.46	0.38	0.35	0.07	–	Bal.	75	[41]
16.1	4.34	3.81	0.87	0.71	0.32	0.03	0.1	Bal.	62	[42]
16.5	4.01	3.88	0.64	0.57	0.34	0.02	0.02	Bal.	62	[42]
16.93	4.17	3.56	0.58	0.62	0.21	–	–	Bal.	49	[43]
16.1	4.34	3.81	0.87	0.71	0.32	0.03	0.1	Bal.	62	[44]
17.13	4.66	4.3	0.54	0.56	0.31	0.041	–	Bal.	65	[16]
16.51	4.35	3.95	0.62	0.73	0.17	0.028	0.088	Bal.	52	[45]

3. The martensite start (M_s) temperature, which is the critical component of the martensitic transformation, is determined using the Ishida model [46] and is imposed as a go/no go condition of M_s temperature being above 200 °C. This is to ensure full transformation of austenite to martensite upon ultrafast cooling of LPBF.
4. The ferrite to austenite transformation temperature must be higher than 1325 °C to ensure minimum retention of δ-ferrite upon printing.
5. In order to create the Cr-rich corrosion-resistant layer, the matrix must contain at least 12 wt.% of Cr at the ageing temperature (considered to be 480 °C) after precipitation [47].
6. The precipitation strengthening contribution of the Cu precipitates is computed through Thermo-Calc, where the product of $f_v^{1/2}\Delta G^{1/2}$ is maximised [47]. f_v and ΔG are the volume fraction of the precipitates and the driving force for formation of such precipitates, respectively. To identify the ideal alloy composition in an efficient manner, the above-described evaluation of a single candidate solution is incorporated in a GA.

3. Materials and experimental methods

3.1. Powder production and additive manufacturing

Gas atomised GA-designed (17-4 mod hereafter) and commercial 17-4 PH SSs powder with spherical morphology were provided by Globus Metal Powders and utilised in this study. Both the alloys were produced under industrial rather than laboratory conditions, supporting the strength of our genetic design methodology. The powder chemical compositions are listed in Table 4. The final optimised parameters of the 17-4 mod composition are:

1. The STR is 61 °C (calculated by Thermo-Calc).
2. The PI is 1.77×10^6 MPa·K (details are provided in [35]).
3. The M_s is 212 °C (Calculated by Ishida model [46]).
4. The ferrite to austenite transformation temperature is 1387 °C (calculated by Thermo-Calc).
5. The Cr concentration in the matrix at ageing temperature (480 °C) is 13.5 wt.% (calculated by Thermo-Calc).
6. The precipitates strengthening factor for the optimised composition is 56 $J^{1/2}$. The average of this factor for the previously LPBFed 17-4 PH SS compositions (listed in Table 3) that were reported in the literature is 44 $J^{1/2}$ (calculated by Thermo-Calc).

Using LPBF equipment (Renishaw AM125), cubic shaped samples with dimensions of $10 \times 5 \times 5$ mm^3 for microstructural characterisation and tensile testing samples (according to ASTM E8 standard dimensions) for mechanical testing were fabricated. The laser beam had a diameter of 44 μm and the process parameters are shown in Table 5. To reduce the residual stress, a multi-directional meander scan strategy was adopted, in which the laser scan direction was rotated by 67° for each layer.

3.2. Microstructural characterisation

Using optical microscopy (OM) and scanning electron microscopy (SEM, FEI Quattro S), the ground cubic samples were polished and etched for microstructural characterisation. The samples were electrochemically etched using 10% oxalic acid exposed at a voltage of 10 V for 10–20 s at room temperature to reveal the microstructures. The microstructure and crystal orientations were also examined with Electron backscatter diffraction (EBSD) (EDAX Velocity^{TM} Pro) with a step size of 0.15 μm. Chemical segregation of the main alloying elements such as Cr, Ni, Mn, and Cu was investigated using electron probe microanalysis (EPMA, JEOL SUPERPROBE JXA-8900M).

The X-ray diffraction (XRD) analysis was conducted using a Bruker AXS D8 Discover diffractometer, equipped with Co-Kα radiation. The θ–2θ configuration was employed, spanning an angular range from 35 to 135°, using increments of 0.015° and an acquisition time of 1.7 s at each step. Total density of dislocations were calculated from the XRD patterns through analysis of XRD peak broadening by modified Williamson-Hall method [48].

In order to identify the nanometre-sized precipitates and carbides, atom probe tomography (APT) was used. For APT measurements, Focused ion beam (FIB) milling (FEI NOVA200) were applied to fabricate needle-shaped specimens. FIB milled APT specimens were extracted from grain boundary regions with high grain boundary misorientation using the *in situ* lift-out method [49]. APT analyses were performed using a local electrode atom probe (LEAP 4000X HR, CAMECA Instrument) in pulsed laser mode at a specimen base temperature of 50 K. The laser pulse energy and frequency were 50 pJ and 125 kHz, and detection rate was 0.5% respectively. Data reconstruction and analyses were done with the IVAS 3.8.16 software provided by CAMECA Instruments.

3.3. Mechanical characterisation

As-printed samples underwent tensile and hardness testing. To determine the average values and standard deviations, the tensile tests were carried out three times. A quasi-static strain rate of 10^{-4} s^{-1} was used for tensile testing using an Instron universal tensile testing equipment. Using a Vickers indenter with 1 kg load and 10 s dwell time, microhardness measurements were carried out based on 20 indentations from various locations of the cubic samples.

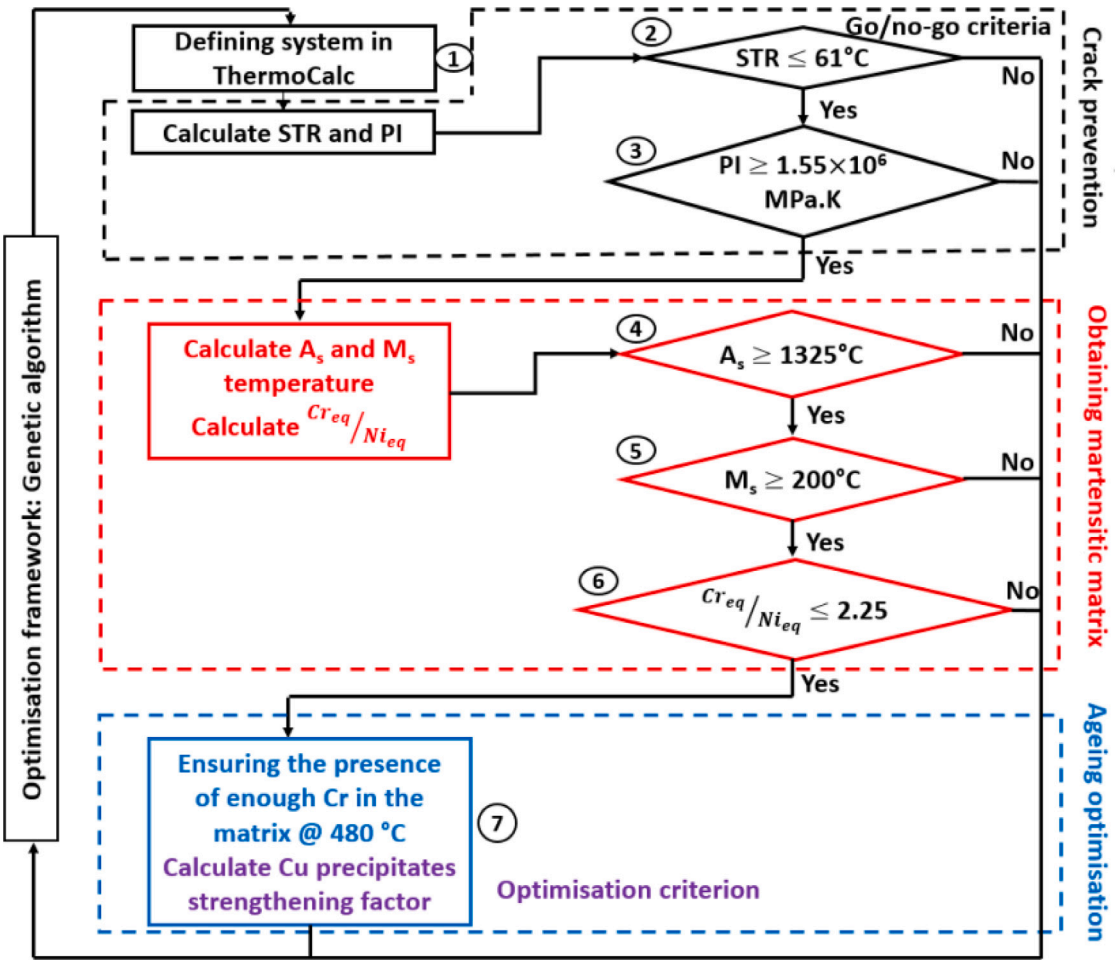

Fig. 1. Genetic algorithm combined with thermodynamic calculations flowchart used in this study to design a novel PH SS.

Table 4
Chemical composition of 17-4 mod and 17-4 PH SSs in wt.%.

Material	Cr	Ni	Cu	Nb	Mn	Si	C	N	Fe
17-4 PH	15.44	5.03	3.19	0.31	0.51	0.51	0.04	0.035	Bal.
17-4 mod	13.59	3.94	5.59	0.5	0.23	0.66	0.02	0.03	Bal.

Table 5
LPBF process parameters used in fabrication of 17-4 mod and 17-4 PH SSs.

Laser power (W)	Scan speed (mm/s)	Hatch distance (mm)	Layer thickness (mm)
180	300	0.075	0.03

4. Results

4.1. Microstructure

The optical microstructures of the as-built samples are depicted in Fig. 2, when seen from build direction and cross section. Melt pool boundaries were clearly visible in both alloys, but the grain structure was not evident in the 17-4 mod alloy due to its ultra-fine grain structure.

Fig. 3 displays the microstructures of both alloys observed by SEM. Cellular structures dominated the microstructure of both alloys. In the original alloy microstructure, very large grains were observed (Fig. 3b), which are characterised as δ-ferrite, whereas the microstructure of the modified alloy represent a fully martensitic matrix (Fig. 3a).

The EBSD crystallographic investigation of the modified and original alloys are shown in Fig. 4. The ultra-fine structure of the 17-4 mod can be recognised in comparison with 17-4 PH alloy. The average grain size of 17-4 mod (calculated from EBSD) was 4 ± 2 μm, which was significantly finer than that of 17-4 PH, which was 44 ± 5 μm (calculated from optical microscopy and SEM) indicating that modification of chemical composition resulted in the development of more refined grains. Such refinement can be attributed to the nucleation and recrystallisation of grains in overlapping areas of various line scans as a result of multiple heating and cooling cycles [50–52]. Figures 4a and b display the EBSD phase maps. A fully body centred cubic (BCC) structure is observed in both alloys in the as-built state. This is further confirmed via XRD patterns presented in Fig. 5, where no face-centred cubic (FCC) peaks can be recognised in the as-built state in both alloys; i.e. no austenite was present. Due to the ultra-fast cooling rate of the melt pool during printing, δ-ferrite can be retained in the as-built samples [53]. δ-ferrite grains must be very coarse [54]. Coarse δ-ferrite grains can be found in the centre of the melt pools of the 17-4 PH (Figs. 2d and 3b), whereas martensite is formed as a result of numerous thermal cycles of remelting in the overlapping melt pools

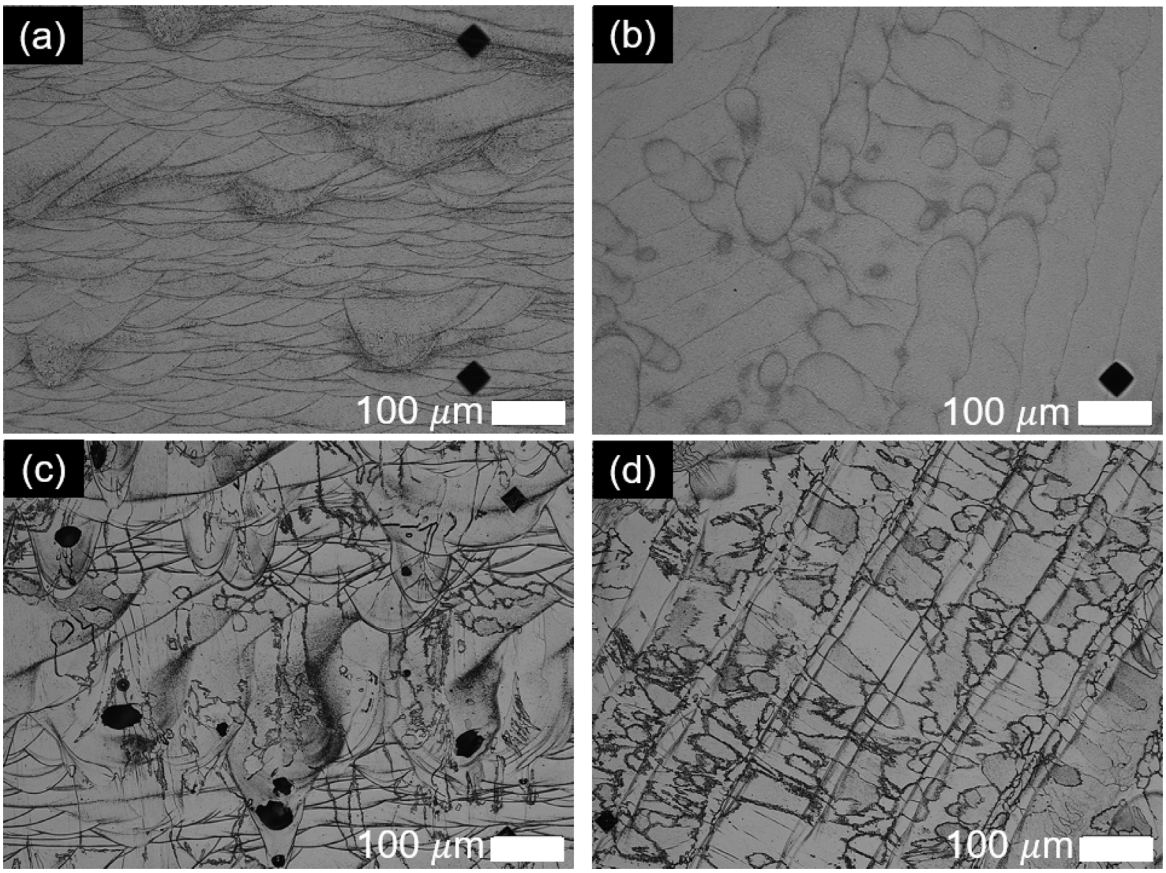

Fig. 2. Optical micrographs showing microstructure of the as-built (a) 17-4 mod in the build direction, (b) cross section of 17-4 mod, (c) 17-4 PH in the build direction, and (d) cross section of 17-4 PH.

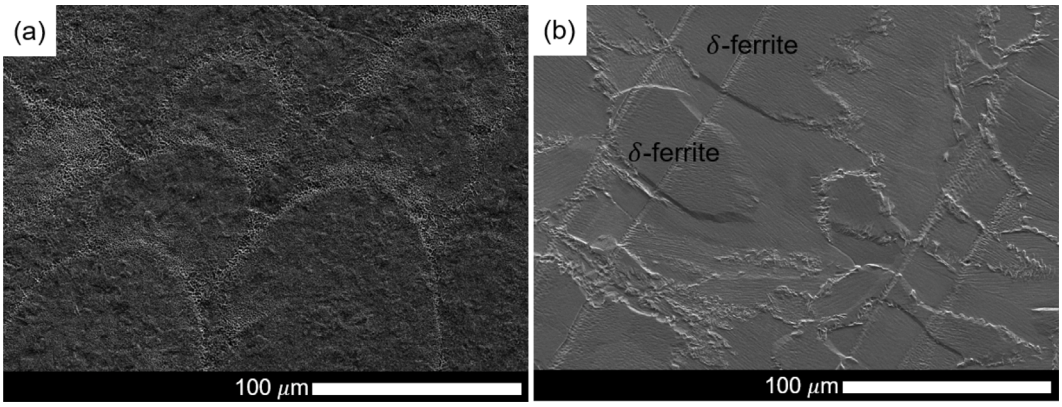

Fig. 3. SEM characterisation of as built (a) 17-4 mod and (b) 17-4 PH alloys.

(Fig. 3a) in the 17-4 mod. As shown in Fig. 4a, the ultimate martensite morphology inherits the recrystallised prior austenite grain [55].

The inverse pole figure (IPF) maps shown in Figures 4c and d demonstrate that an equiaxed microstructure with random texture is developed in both alloys (a lower magnification IPF of 17-4 PH alloy is presented in the supplementary file, Figure S1 to cover more grains).

The distribution of geometrically necessary dislocations (GNDs) in the matrix is shown in Fig. 6. A higher density of GNDs can be observed in martensite grains in 17-4 mod alloy (Fig. 6a), whereas a lower GND density is characterised in large ferrite grains in 17-4 PH alloy (Fig. 6b). This further indicates how two BCC structures are correctly described. The average GND density of the 17-4 mod and 17-4 PH are 2.2×10^{15} m^{-2} and 7.8×10^{13} m^{-2}, respectively. Total dislocation density, which consists of GNDs and statistically stored dislocations (SSDs), was also measured via modified Williamson-Hall approach [48] from the XRD patterns. The measured values were $1.5\pm0.2\times10^{15}$ m^{-2} and $8.3\pm0.2\times10^{14}$ m^{-2} for 17-4 mod and 17-4 PH, respectively in the as-built state. Since XRD beams cover a larger surface of the specimen compared to EBSD, where the characterisation is more local and only GND dislocation density can be measured, it can be concluded that almost all of the dislocations in 17-4 mod are GNDs, however, the majority of dislocations in 17-4 PH are SSDs.

The phase evolution for both alloys was predicted using thermodynamic calculations at non-equilibrium state using the Thermo-Calc software [34] and TCFE10 database. The melt pool is well mixed at an ultrafast cooling rate during solidification in LPBF, which supports the employment of the Scheil simulation. As can be observed in Figs. 7a

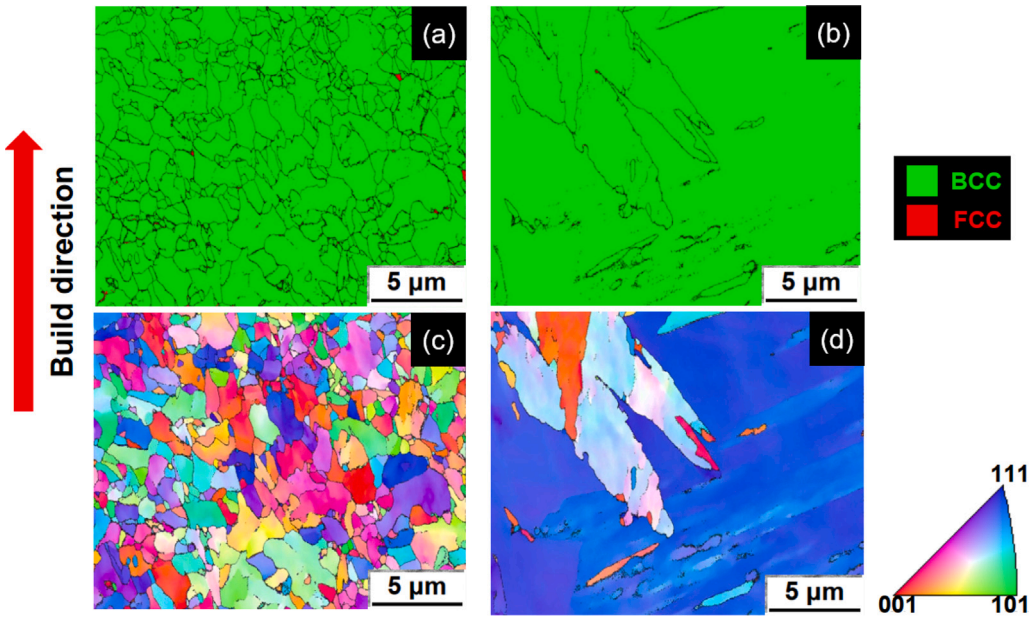

Fig. 4. EBSD phase maps of as-built (a) 17-4 mod and (b) 17-4 PH alloys. Green and red colours represent BCC and face centred cubic (FCC) phases, respectively. IPF maps of (c) 17-4 mod (d) 17-4 PH are also exhibited.

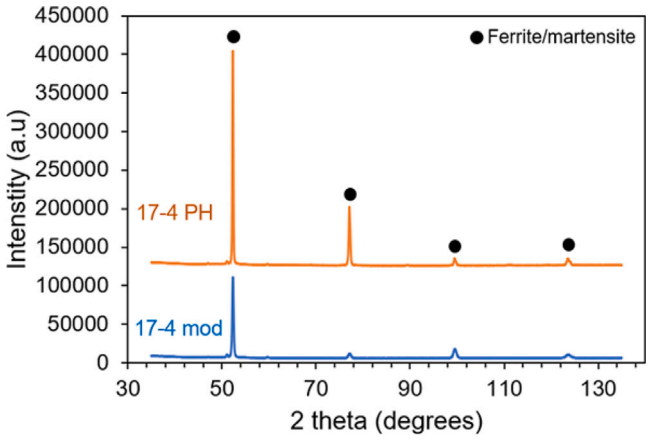

Fig. 5. XRD patterns of both 17-4 mod and 17-4 PH alloys in the as-built state.

and b, the solidification path of the two printed alloys are completely different. In 17-4 mod, austenite is the primary solidified phase. After about 90% completion of solidification, Nb(C,N) and δ-ferrite begin to form in 17-4 mod. However, the main solidification phases in 17-4 PH are both austenite and δ-ferrite. Figs. 7c and d show that there is almost no retained δ-ferrite upon solidification of 17-4 mod, whereas 30% of δ-ferrite retains at the end of solidification of 17-4 PH. This further confirms the absence and presence of δ-ferrite in as-built 17-4 mod and 17-4 PH, respectively.

The melt pool boundaries are one of the preferred sites for nano-precipitate formation. According to EPMA analysis (Figs. 8 and 9), Mn and Cu segregated mostly to the melt pool boundaries in 17-4 mod, whereas there is no significant segregation of any alloying elements to the melt pool boundaries of 17-4 PH.

Fig. 10 displays the results of the APT analysis of as-printed 17-4 mod steel along a high-angle grain boundary, which is shown as region of interest (ROI) in the EBSD IPF map in Fig. 10a. Significant segregation of Cu, Nb, and C atoms were visible in the APT maps (Fig. 10b).

Table 6
Chemical composition of the matrix and Cu-rich precipitates in as-built 17-4 mod measured by APT.

Element	Matrix (at.%)	Cu-rich precipitates (at.%)
Fe	78.60 ± 0.03	54.00 ± 0.12
Cr	14.70 ± 0.01	9.43 ± 0.04
Ni	3.21 ± 0.06	3.88 ± 0.02
Cu	1.00 ± 0.01	29.70 ± 0.08
Mn	0.23 ± 0.02	0.5 ± 0.09
Nb	0.26 ± 0.02	0.62 ± 0.01
Si	1.73 ± 0.04	1.34 ± 0.01
C	0.07 ± 0.00	0.19 ± 0.01

Table 7
Chemical composition of the matrix and Nb-rich precipitates in as-built 17-4 mod measured by APT.

Element	Matrix (at.%)	Nb-rich precipitates (at.%)
Fe	78.60 ± 0.04	5.20 ± 0.24
Cr	14.70 ± 0.01	8.10 ± 0.31
Ni	3.21 ± 0.01	1.10 ± 0.11
Cu	1.00 ± 0.00	1.50 ± 0.13
Mn	0.23 ± 0.00	0.11 ± 0.03
Nb	0.26 ± 0.00	48.30 ± 0.89
Si	1.73 ± 0.00	–
C	0.07 ± 0.00	20.20 ± 0.51
N	0.016 ± 0.001	13.30 ± 0.41

In order to investigate the characteristics of precipitates in the as-built 17-4 mod, the computed composition profile of Cu-rich precipitates is displayed in Fig. 11 as a function of distance to the 15 at.% Cu iso-concentration surface (proximity histogram). Cu, Nb, and C form the majority of the Cu-rich precipitates core, which suggests that Fe and Cr atoms were moved from the core to the matrix, where their concentrations drastically fell to 54 and 9.43 at.% from 78.6 and 14.7 at.%, respectively (Table 6).

Fig. 12 shows the distribution of Nb, C, and *N* atoms to provide further clarity on synergistic alloying segregations. These results demonstrated that Nb(C,N) are also developed along adjacent to Cu precipitates during LPBF. They have bigger sizes compared to Cu precipitates. Additionally, as opposed to spherical morphology of Cu-precipitates, Nb(C,N) display an elongated morphology. The concentration of various alloying elements in the Nb(C,N) core and the matrix

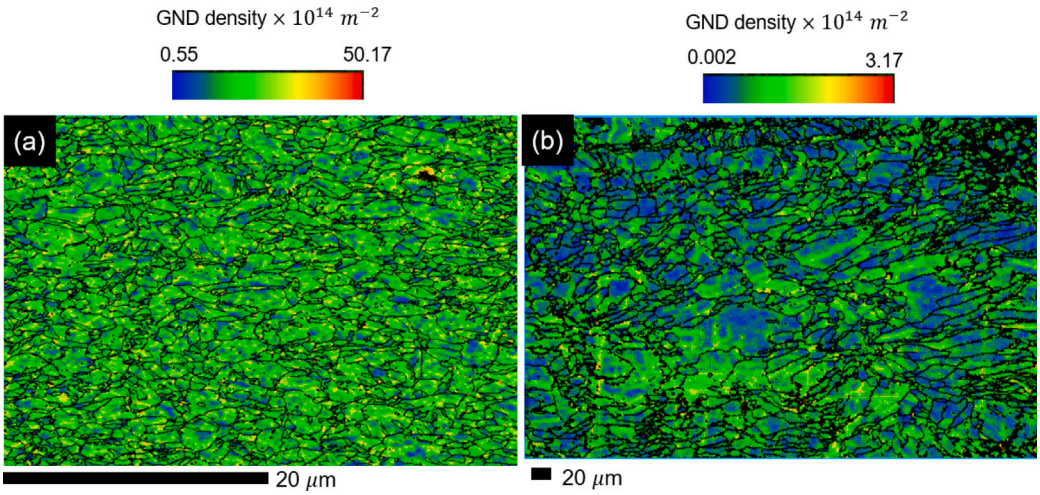

Fig. 6. Distribution of GNDs in LPBF as-built (a) 17-4 mod and (b) 17-4 PH.

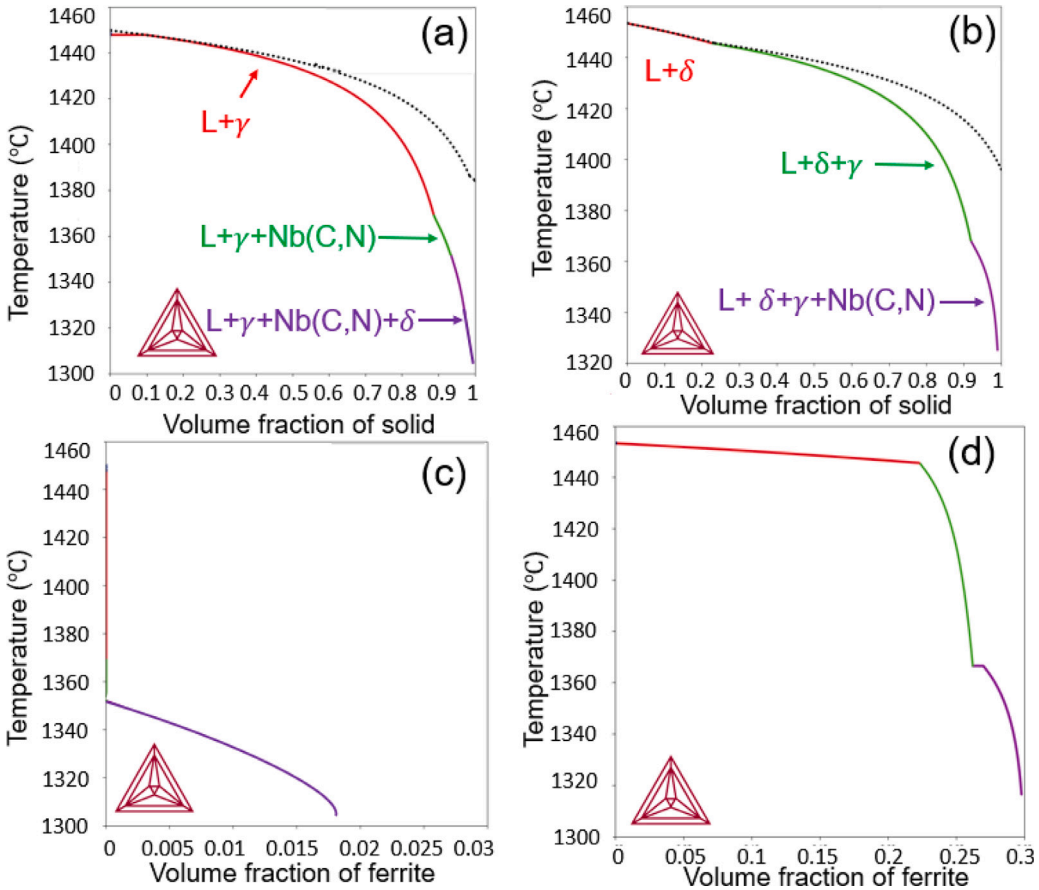

Fig. 7. Non-equilibrium Scheil solidification simulation of (a) 17-4 mod and (b) 17-4 PH steels. The predicted amount of δ-ferrite upon completion of solidification of (c) 17-4 mod and (d) 17-4 PH are also shown.

are shown in the proximity histogram (Fig. 12b) and listed in Table 7. Nb-rich precipitates had larger concentrations of Nb, C, and N.

4.2. Mechanical properties

In order to assess the mechanical properties of the as-built 17-4 mod with regard to its distinct microstructural features, tensile and hardness tests were performed. Representative engineering stress–strain curve of room temperature deformed as-built 17-4 mod is shown in Fig. 13a. The ranges of yield and ultimate tensile strength (UTS) of commercial 17-4 PH and 15-5 PH in the as-built state (Table 1) are shown in Fig. 13b for comparison. The average yield strength, UTS, uniform elongation (UEL), total elongation (TEL), and hardness values are listed in Table 1. The novel 17-4 mod alloy exhibited the highest yield and UTS compared to any commercial 17-4 PH and 15-5 PH alloys that has been reported. For hardness comparison, the 17-4 PH alloy in this study has been tested. A hardness of 313 ± 6 has achieved, which is far lower than the modified alloy. It is worth mentioning that this improvement in yield, UTS and hardness is obtained without compromising ductility (Tables 1). Based on Table 1 mechanical properties of 17-4 mod alloy

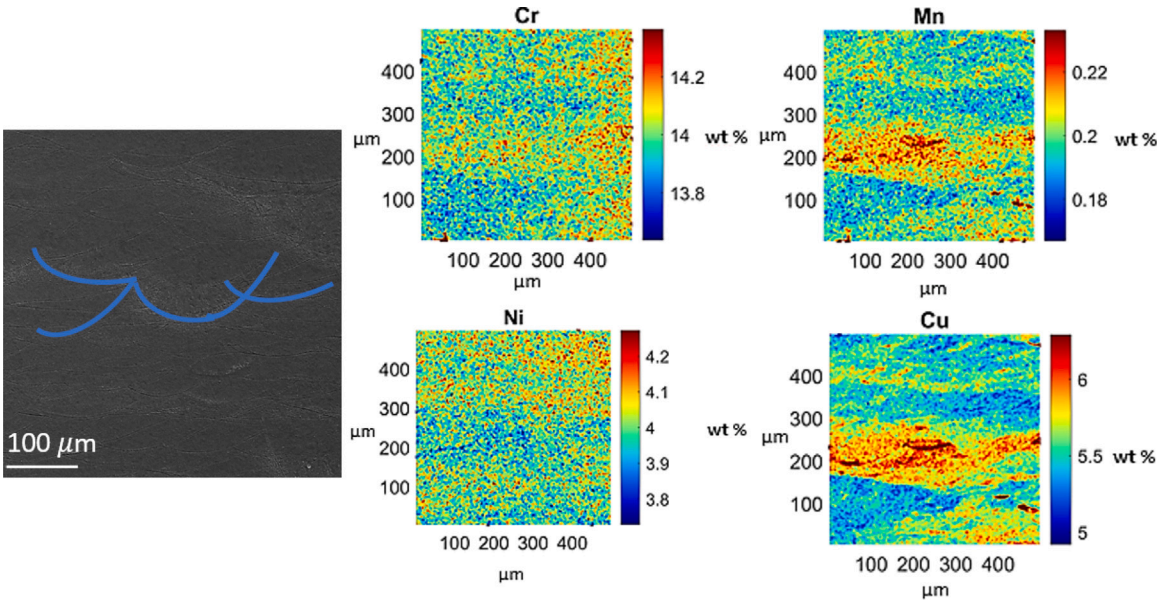

Fig. 8. SEM micrograph and corresponding EPMA mapping results of the as-printed 17-4 mod.

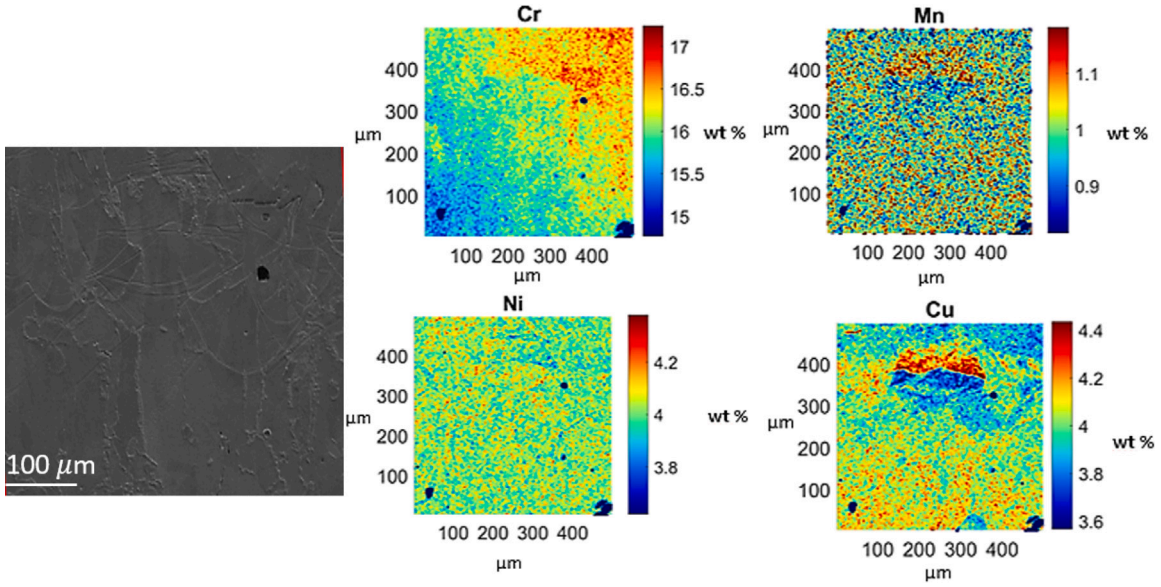

Fig. 9. SEM micrograph and corresponding EPMA mapping results of the as-printed 17-4 PH.

is comparable with 17-4 PH and 15-5 PH alloys in wrought conditions (solution annealed and aged). This further proves the capability of adopting LPBF to produce PH alloys with superior mechanical properties compared to their wrought counterparts, without the need for subsequent heat treatment.

Since AMed components are produced near-net shape, and there is no need for further deformation to achieve the final geometry, plasticity mechanisms of the present alloys are not presented in this work, and a comparison to wrought counterparts is not shown in Fig. 13b.

5. Discussion

5.1. Microstructure evolution and grain refinement

To determine the origin of the microstructures in the as-printed condition, the metallurgical evolution of these steels is examined during solidification. 17-4 PH typically solidifies primarily as δ-ferrite phase; due to solid-state diffusion, the δ-ferrite eventually transforms into austenite during cooling, and then austenite transforms into martensite at temperatures below the martensitic start temperature [56]. As seen in Figs. 7a and b, although the primary solidifying phase during LPBF of 17-4 PH alloy is δ-ferrite, 17-4 mod solidifies primarily as austenite. Typically, the solidification mode of SSs is significantly influenced by the Cr_{eq}/Ni_{eq} ratio [57]:

$$Cr_{eq}(wt.\%) = Cr + 2Si + 1.75Nb, \tag{1}$$

$$Ni_{eq}(wt.\%) = Ni + 0.5Mn + 0.3Cu + 25N + 30C. \tag{2}$$

For 17-4 PH and 17-4 mod, the calculated Cr_{eq}/Ni_{eq} ratios were 2.08 and 2, respectively. It has been reported that during pulsed laser welding, where the cooling rate and solidification conditions are similar to LPBF, the crucial Cr_{eq}/Ni_{eq} value for a transition between austenitic and ferritic solidification is 1.7 [58], which suggests that both alloys in the present study should solidify through a primarily ferritic phase.

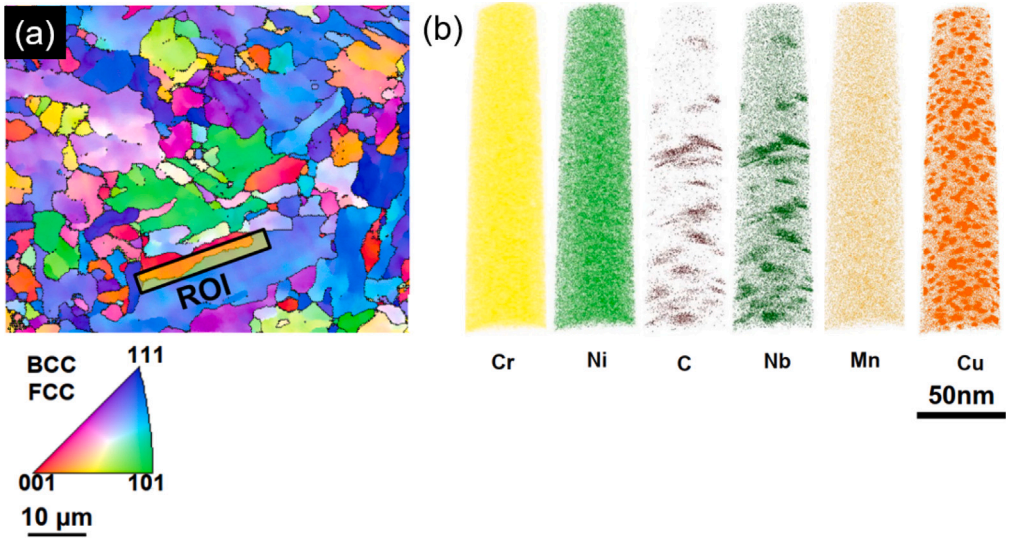

Fig. 10. (a) EBSD IPF map of the as-printed 17-4 mod steel, showing the region of interest (ROI) that APT maps are taken from. (b) APT maps of as-printed 17-4 mod showing Cr, Ni, C, Mn, Nb, and Cu elements.

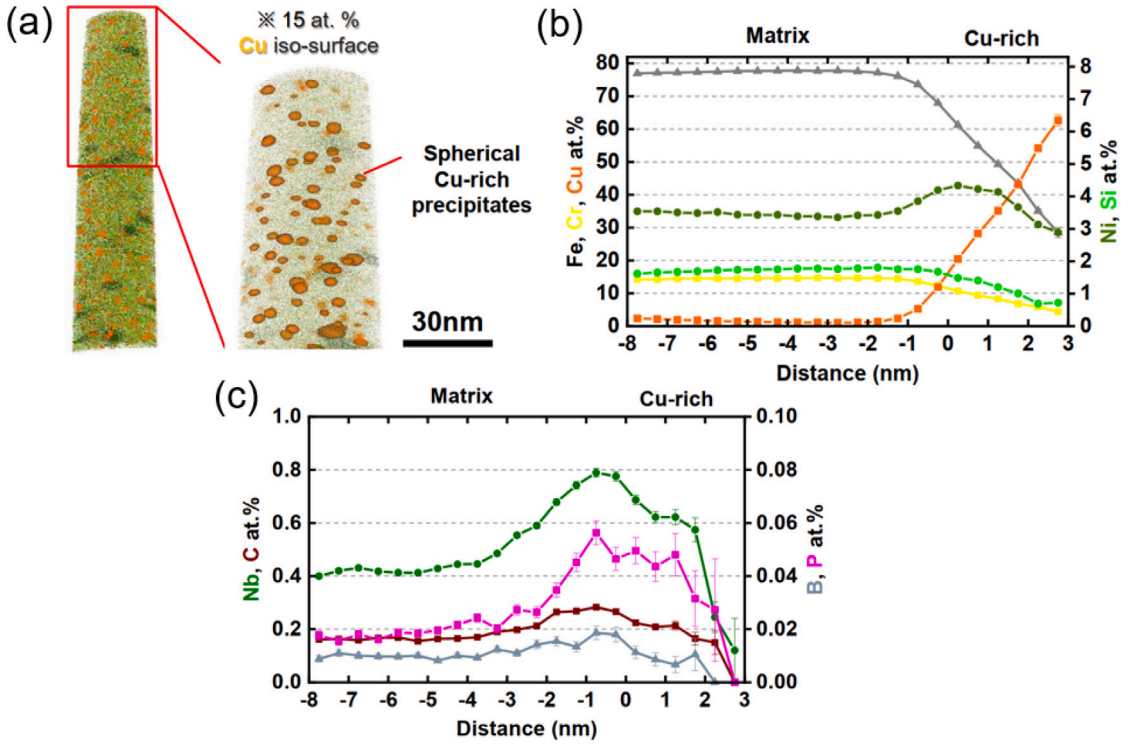

Fig. 11. (a) Cu-rich precipitates focusing on iso-concentration surfaces with 15 at.% Cu (orange). (b) and (c) Proximity histogram of Cu-rich precipitates and the matrix.

However, the results of this study reveal that Cr_{eq}/Ni_{eq} is not a useful means to predict the solidification mode of PH steels during LPBF. In 17-4 mod Cr, Cu, and Nb are the elements that are outside of the nominal chemical composition range of commercial 17-4 and 15-5 PH steels. Scheil simulations via ThermoCalc show that Cu is the key element in the determination of the solidification mode of PH SSs. Scheil simulations revealed that the threshold weight percentage of Cu in 17-4 mod alloy to change the solidification mode from primary ferrite to primary austenite is 4.3 wt.%, which is the maximum amount of Cu in commercial 17-4 and 15-5 PH SSs. It is also shown that Nb and Cr can vary from 0.1-0.5 wt.% and 13-17 wt.% without any limitations. Therefore, an increase in the Cu to 5.59 wt.% in this study without a change in Cr_{eq}/Ni_{eq} led to elimination of δ-ferrite at the end of solidification.

Furthermore, the formation of Nb(C,N) during solidification can inhibit austenite grain growth at high temperatures due to the low solubility of Nb(C,N) in austenite [29]. Therefore, addition of Cu and formation of Nb(C,N) are the main grain refinement mechanisms during LPBF of 17-4 mod alloy.

An analysis of the grain orientation of the samples can help to further validate the existence of a primary austenitic solidification mode in 17-4 mod alloy. Recent studies show that having a strong texture demonstrates that the matrix phase is still the phase in which the material is solidified [59]. Since δ-ferrite grains are predominantly solidification structures, they must show a strong ⟨100⟩ texture, because

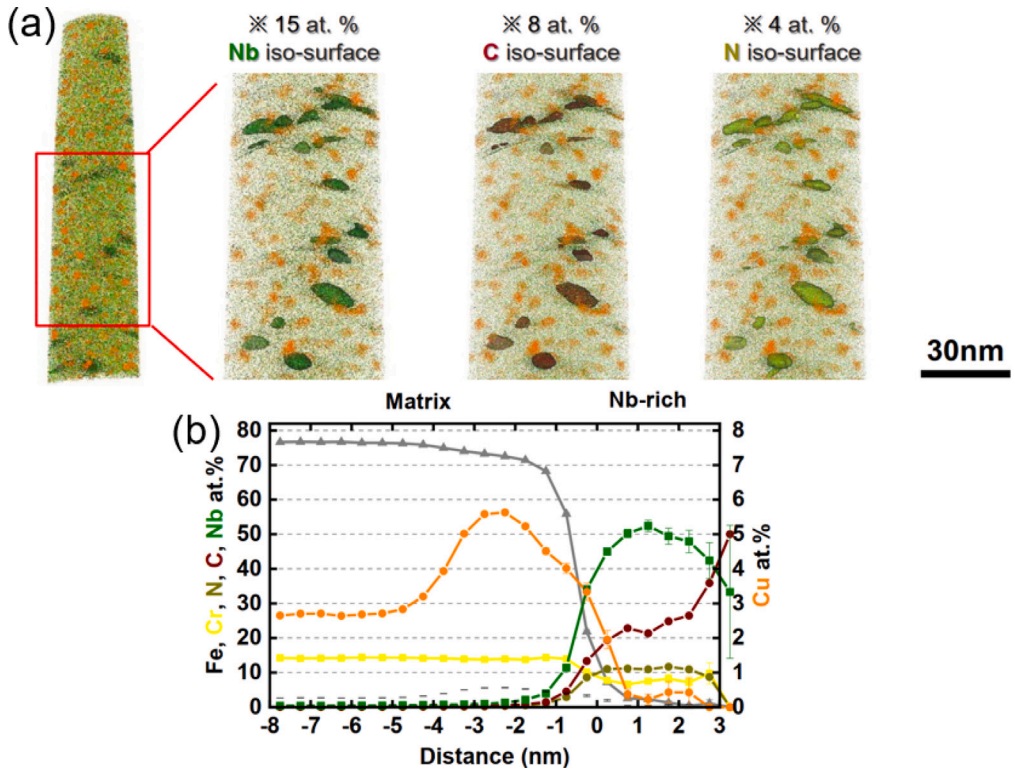

Fig. 12. (a) Nb-rich precipitates focusing on iso-concentration surfaces with 15 at.% Nb (green), 8 at.% C (red), and 4 at.% *N* (light green). (b) Proximity histogram of Nb-rich precipitates and the matrix. (For interpretation of the references to color in this figure legend, the reader is referred to the web version of this article.)

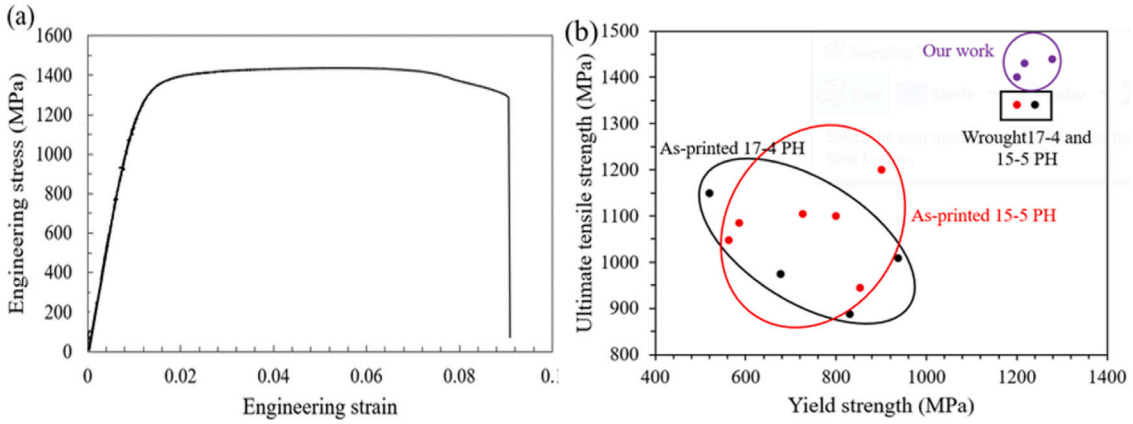

Fig. 13. (a) Representative tensile stress–strain curve of as-built 17-4 mod. (b) Comparison of the mechanical yield strength and the ultimate tensile strength of 17-4 mod with as AMed 17-4 PH and 15-5 PH, as well as wrought 17-4 PH and 15-5 PH alloys (reported in literature and listed in Table 1).

solidified grains during LPBF frequently grow in ⟨100⟩ directions [59]. According to Figure S1 (supplementary material), the majority of coarse grains in 17-4 PH steel display a texture of ⟨100⟩. This also suggests that ⟨100⟩ grains in 17-4 PH are δ-ferrite. Since the cooling rate during LPBF is very large ($\sim 10^6$ K/s), there is no sufficient time for transformation of δ-ferrite to austenite. Therefore, in 17-4 PH, all the δ-ferrite that is formed at the end of solidification is retained after the component is built. This texture would have been significantly diminished if any solid-state transitions, such as the δ-ferrite into austenite and austenite to martensite transformations had occurred, since new grains of the new phase would have formed inside parent grains of the previous phase. 17-4 mod microstructure displays a random texture (Fig. 4c), which suggests that such grains are prior austenite grains, which transform into martensite during LPBF.

5.2. Effect of microstructure on mechanical properties

The main strengthening contributions in wrought PH steels are precipitation and grain boundary strengthening [4]. However, due to very high dislocation density of AM-produced components, dislocation strengthening also plays a major role towards yield strength (σ_Y) of such steels. Therefore, σ_Y for 17-4 mod alloy can be calculated through:

$$\sigma_Y = \sigma_f + \sigma_{ss} + \sigma_{gb} + \sigma_\rho + \sigma_p, \tag{3}$$

where σ_f is the friction stress, σ_{ss} is the solid solution strengthening, σ_{gb} is the grain boundary strengthening, σ_ρ is the dislocation hardening, and σ_p represents the contribution of precipitates into hardening. σ_f can be estimated via [60]:

$$\sigma_f = M\tau_{CRSS}, \tag{4}$$

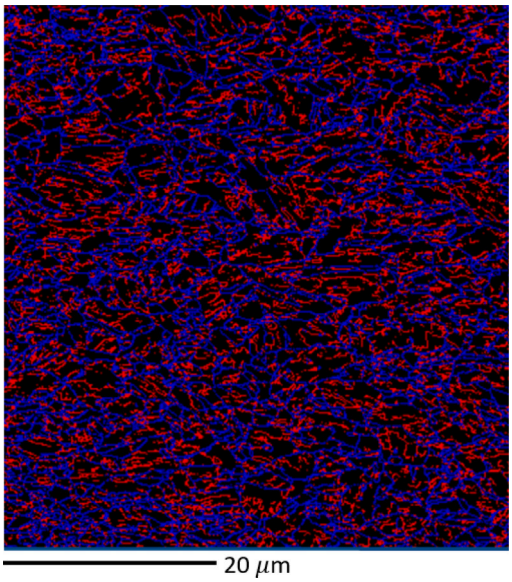

Fig. 14. EBSD grain boundary map, illustrating the distribution of HAGBs (shown in blue) and LAGBs (shown in red). (For interpretation of the references to color in this figure legend, the reader is referred to the web version of this article.)

where $M = 2.5$ [61] is the Taylor factor and $\tau_{CRSS} = 25$ MPa [62] is the Peierls-Nabarro stress of pure iron. Therefore, σ_f is 62 MPa for as-built 17-4 mod.

σ_{ss} can be estimated via [63]:

$$\sigma_{ss} = 77\sqrt{W_N} + 20W_{Mn} + 7W_{Cr} + 33W_{Si} + 2.9W_{Ni}, \quad (5)$$

where Wi (i refers to each alloying element) is the amount of each element in the solid solution in wt.% (Table 4). Since the matrix is martensitic, chemical composition of martensite presented in Table 6 (a conversion of values from at.% to wt.% has been carried out), is used to estimate the contribution of σ_{ss}. σ_{ss} is estimated to be 141 MPa.

According to the Hall-Petch relationship, the yield strength is inversely related to the square root of the grain size. However, since 17-4 mod is a fully-martensitic alloy, the martensite block size (d_{block}) is the microstructural feature that controls σ_{gb} [64]. Therefore, σ_{gb} can be calculated via [64]:

$$\sigma_{gb} = \frac{k}{\sqrt{d_{block}}}, \quad (6)$$

where k=190 MPaμm$^{-1/2}$ [65] for martensite block boundaries. In fully martensitic microstructures, the martensite block size is approximately equal to the subgrain size (low-angle grain boundaries). The distribution of low-angle grain boundaries (LAGBs, where the misorientation is between 2° and 15°) and high-angle grain boundaries (HAGBs, where the misorientation is larger than 15°) are shown in Fig. 14. The average martensite block size is 2.52±0.5 μm. Therefore, the contribution of σ_{gb} is about 120 MPa into the total yield strength.

The strengthening contribution of dislocations can be quantified using Taylor relationship:

$$\sigma_\rho = M\alpha Gb\sqrt{\rho}, \quad (7)$$

where $M = 2.5$ is the Taylor factor [61], $\alpha = 0.2$ [66] is a constant, $G = 76$ GPa is the shear modulus of lath martensite [65], $b = 0.25$ nm is the magnitude of the Burgers vector, and ρ is the dislocation density. According to the XRD data, the total dislocation density is 1.5×10^{15} m^{-2}, and thus, $\sigma_\rho = 367$ MPa. It must be noted that the dislocation density measurements from XRD technique were used here rather than the GND density calculated from EBSD to quantify the strengthening contribution of dislocations. Since XRD covers a much larger volume of the sample compared to EBSD and it has the ability to capture both types of dislocations (GNDs and SSDs), leading to a better averaged dislocation density measurement, the data from this method have been used to quantify dislocation hardening in this study.

The contribution of Cu precipitates into strengthening can be modelled via [4]:

$$\sigma_P = \frac{M\alpha Gb\sqrt{f_{Cu}}}{1.77r}, \quad (8)$$

where f_{Cu} is the volume fraction of Cu precipitates and r is the mean radius of the precipitates. According to the APT results, $r = 1.05 \pm 0.46$ nm and $f_{Cu} = 0.011$. Therefore, the contribution of precipitates to the total strengthening of 17-4 mod is about 536 MPa. In here, the contribution of Nb(C,N) is not considered, since their number is not enough to make a significant contribution to strengthening. APT was performed in several regions of the sample to ensure a comprehensive characterisation of precipitates. However, specific analyses were conducted in two distinct regions, both showing similar precipitate distribution and morphology. The size distribution of Cu-rich precipitates was carefully measured, with radius ranging from 1 nm to 34 nm, consistent with findings from studies of AMed 17-4 PH SS as reported in [14,67]. This similarity supports the representativeness of our observations across the sample.

Five mechanisms (i) friction stress, (ii) solid solution hardening, (iii) grain boundary strengthening, (iv) dislocation hardening, and (v) precipitation hardening are responsible for yield strengthening of as-built 17-4 mod alloy. Fig. 15 illustrates how each of these mechanisms contributes differently to the yield strength of 17-4 mod alloy. By calculating the relative contributions in Fig. 15a, the pie charts in Fig. 15b summarise the relative percentages of each mechanisms's contribution.

5.2.1. Precipitation hardening

Precipitation hardening is the most important factor in the yield strengthening of 17-4 mod, accounting for approximately 44% of yield strength, as shown in Fig. 15b. Precipitation of Cu-rich particles are reported previously in as-printed commercial 17-4 PH [14,67]. Guo et al. [67] characterised the presence of Cu precipitates with average size of about 4 nm in an LPBFed as-built 17-4 PH processed with a very high laser power (520 W). They claimed that intrinsic heat treatment during LPBF as a result of cyclic heating and cooling can induce formation of such precipitates. However, the volume fraction and size of those precipitates depends significantly on LPBF process parameters. In addition, Nb(C,N) particles are also characterised in the present work to be formed during the solidification of 17-4 mod. Although, the results of this study shows no direct contribution of Nb(C,N) into precipitation hardening (due to their large size and low volume fraction), they can contribute to grain refinement, and subsequently in yield strengthening of 17-4 mod in the as-built condition.

5.2.2. Dislocation strengthening

In the 17-4 mod alloy, the dislocation strengthening is the second most significant mechanism, accounting for approximately 30% of the yield strength. According to the Kocks-Mecking theory, the competition between multiplication and annihilation of dislocations determine the dislocation density of alloys after processing. Therefore, the evolution of dislocation density of alloys during printing can be described via [68]:

$$d\rho/d\gamma = \frac{k_1}{b}\sqrt{\rho} - f\rho, \quad (9)$$

where γ is the strain, k_1 is the dislocation multiplication factor, and f is the dynamic recovery coefficient. Since recovery and recrystallisation are competing phenomena, alloys with a larger f have lower recrystallisation rate. k_1 is a constant that does not change with temperature and strain. Therefore, the dislocation density controlling variables are the dislocation density at each thermal cycles and the f. Lath martensite

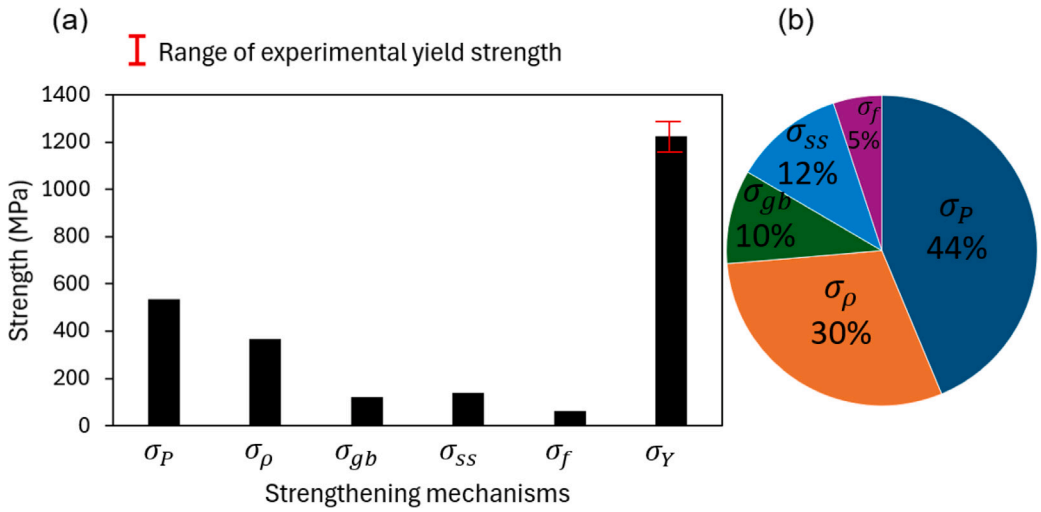

Fig. 15. (a) Contribution of various strengthening mechanisms to yield strength of as-built 17-4 mod. The range of the experimental yield strength is shown by a red error bar. (b) Pie charts representing the percentage of contribution of each strengthening mechanisms into yield strengthening.

typically has a high dislocation density of about 10^{15} m^{-2}, whereas ferrite usually has a much lower dislocation density [69]. When the carbon content of the alloy is low, the lath martensite has the potential to undergo recrystallisation in addition to recovery during tempering, because the dislocation density is high enough to promote recrystallisation [70]. However, recrystallisation of martensite is a static, discontinuous, and inhomogeneous process [70]. In contrast, a heavily deformed ferritic structure undergoes recrystallisation much faster and more homogeneously [71]. Therefore, f for a ferritic microstructure must be lower than a martensitic structure. Galindo-Nava and Rivera-Díaz-del-Castillo [72] quantified f for BCC microstructures and showed that the only microstructure-dependent parameter that can affect f is the shear modulus, which is inversely proportional to f. Since the shear modulus of lath martensite (76 GPa [65]) is lower than the shear modulus of ferrite (80 GPa [65]), a ferritic structure has a lower f and higher recrystallisation rate compared to a martensitic structure. Therefore, shear modulus can be used as an effective means to design LPBF alloys with higher dislocation strengthening.

Recrystallisation behaviour of ferrite and martensite should differ since their substructures are different significantly from one another. Fig. 16 illustrates the EBSD grain orientation spread (GOS) maps of 17-4 mod and 17-4 PH in the as-built condition. GOS is a method for measuring in-grain misorientations. By computing the misorientation between each data point within a grain and the average orientation of that grain, a GOS value is assigned to each grain. A threshold of 2° is often utilised to identify recrystallised grains [73]. The GOS of grains was used in this study to determine recrystallised grains. Recrystallised grains (having a GOS of less than 2°) are shown in blue in Figs. 16a and b. The percentage of recrystallised grains in 17-mod and 17-4 PH in as-built condition are 22% and 51%, respectively. Since the LPBF processing parameters are the same for both alloys, the fraction of recrystallised grains is in agreement with previous reports claiming that the required time for recrystallisation of ferrite is almost half of martensite [70]. In this study, the fraction of recrystallised grains is almost twice in the ferritic microstructure (17-4 PH) compared to martensitic structure (17-4 mod).

5.2.3. Synergy between precipitation, dislocation, and grain boundary strengthening

The GA is utilised primarily as an optimisation tool within our computational alloy design framework. It selects the optimal alloy compositions aimed at maximising mechanical properties while ensuring good printability. Maximisation of strength is achieved by obtaining a fully martensitic matrix upon printing, which leads to enhanced properties due to high dislocation density of martensitic structures and promotion of precipitation hardening during LPBF. Therefore, GA does not directly maximise the strength, but it finds the optimal compositions within a certain composition range, which results in a fully-martensitic matrix that is printable. This subsequently will lead to maximisation of strength.

In the 17-4 mod alloy, the synergy between precipitation, dislocation, and grain boundary strengthening significantly contributes to its microstructure evolution and mechanical properties. The solidification process and the resulting microstructure in similar steels such as 17-4 PH are influenced by the Cr_{eq}/Ni_{eq} ratio, typically indicating a primarily ferritic phase. However, deviations in alloy composition, particularly the elevated Cu content in 17-4 mod, shift the solidification mode to primarily austenitic. The addition of Cu, along with the formation of Nb(C,N) during solidification, acts as a key grain refinement mechanism in the alloy, inhibiting austenite grain growth at high temperatures.

In terms of mechanical properties, the alloy's yield strength is influenced by multiple strengthening mechanisms. Precipitation strengthening, with a significant contribution of approximately 44%, arises from the high dislocation density typical in AMed components. The synergy between precipitation hardening and grain boundary strengthening plays a vital role, with Cu precipitates and Nb(C,N) contributing to the overall yield strength. The finer grain size in 17-4 mod, facilitated by the presence of Nb(C,N), enhances grain boundary strengthening. Additionally, precipitation hardening from Cu precipitates further reinforces the material. The collective effect of these mechanisms demonstrates a complex synergy, illustrated in Fig. 15, showcasing the relative contributions of friction stress, solid solution strengthening, grain boundary strengthening, dislocation hardening, and precipitation hardening to the alloy's yield strength.

The analysis of the dislocation strengthening mechanism highlights its importance in the 17-4 mod alloy, emphasising the importance of understanding the dislocation evolution during the printing process. The competition between dislocation multiplication and annihilation, influenced by factors like shear modulus and dynamic recovery coefficient, contributes to the observed dislocation density. Additionally, the disparity in recrystallisation behaviour between ferritic and martensitic structures, as evidenced by EBSD GOS maps, further emphasises the significance of microstructural differences in the alloy's mechanical properties. The study provides valuable insights into the intricate interplay of strengthening mechanisms in AMed alloys, paving the way for tailored alloy design for specific applications.

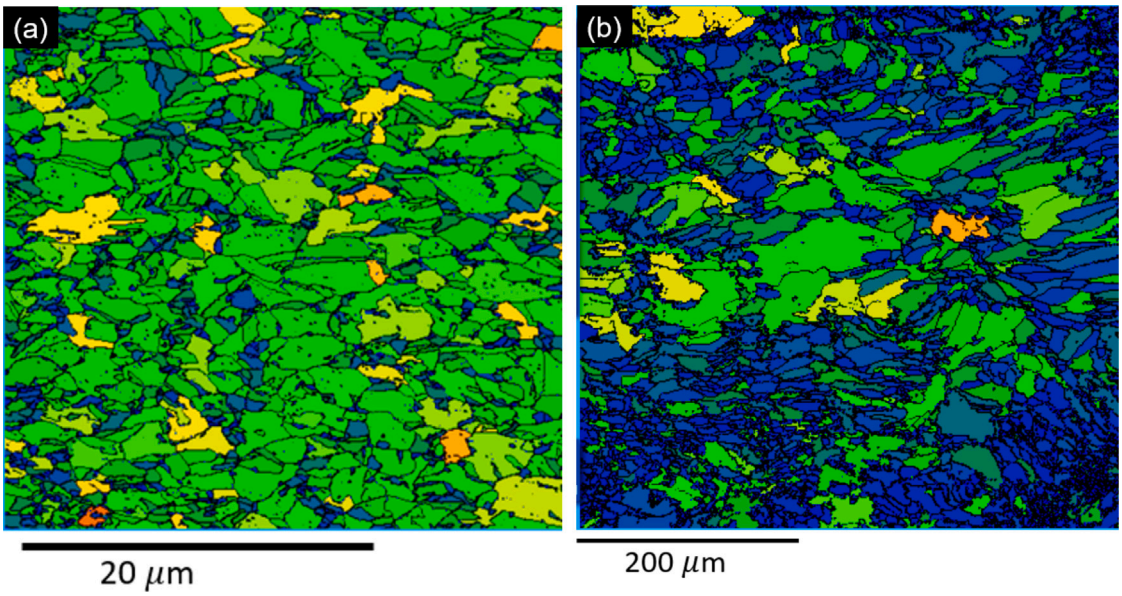

Fig. 16. EBSD GOS maps of (a) 17-4 mod and (b) 17-4 PH alloy in the as-built condition. Blue grains represent recrystallised grains.

6. Conclusions

The microstructure and mechanical properties of a laser powder bed fused (LPBFed) modified 17-4 precipitation hardening (PH) stainless steel (SS) (17-4 mod) and its commercial 17-4 PH alloy counterpart were studied in this work. The following findings were made:

1. Modification of chemical composition of commercial 17-4 PH SS resulted in obtaining a fully refined martensitic microstructure upon LPBF, followed by mechanical properties surpassing those of commercial 17-4 PH SS both in wrought and LPBFed conditions. Increase in the Cu content from 3.19 wt.% in commercial alloy to 5.59 wt.% is responsible to adjust solidification mode and prevention of retained ferrite after LPBF.

2. An increase in Nb content in 17-4 mod led to formation of Nb(C,N) during solidification, which hindered austenite grains to grow upon solidification, resulting in significant grain refinement compared to LPBFed commercial 17-4 PH.

3. Precipitation hardening and dislocation hardening are found as the two main strengthening mechanisms of LPBFed 17-4 mod, where precipitation hardening is determined as the most significant mechanism.

4. The competition between formation of Cu precipitates during LPBF, dislocation multiplication and annihilation, as well as formation of Nb(C,N) during solidification, which enable grain growth inhibition, are the main features to control to achieve an appropriate combination of yield and ultimate tensile strength. Due to the significant influence of shear modulus on the rate of recovery/recrystallisation in ferrite and martensite, this material-dependent physical property can be used to design alloys of desirable microstructures for LPBF.

5. The exceptional mechanical properties of LPBFed 17-4 mod stem from a synergistic interplay among strengthening mechanisms. Refined martensitic microstructure, driven by compositional adjustments and increased Cu content, works in tandem with Nb(C,N) formation to control grain size. The dominance of dislocation multiplication and annihilation, amplified by high dislocation density, emerges as the key contributor to yield strength. Additionally, Cu-rich particle precipitation enhances overall strength. Recognising and optimising these synergies offer insights into tailoring superior properties for AM applications.

CRediT authorship contribution statement

Hossein Eskandari Sabzi: Conceptualization, Data curation, Formal analysis, Investigation, Methodology, Validation, Visualization, Writing – original draft, Writing – review & editing. **Seoung-Ho Lim:** Methodology, Software. **Diego Della Crociata:** Methodology. **Roger Castellote-Alvarez:** Methodology. **Marco Simonelli:** Supervision. **David San-Martín:** Supervision. **Xinjiang Hao:** Funding acquisition, Resources. **Pyuck-Pa Choi:** Supervision. **Pedro E.J. Rivera-Díaz-del-Castillo:** Conceptualization, Funding acquisition, Resources, Supervision, Validation, Writing – review & editing.

Declaration of competing interest

The authors declare that they have no known competing financial interests or personal relationships that could have appeared to influence the work reported in this paper.

Acknowledgements

This work was supported by the Royal Academy of Engineering, United Kingdom (RCSRF1718/5/32), by EPSRC, United Kingdom via DARE grant (EP/L025213/1), and by UKRI, United Kingdom via AM-Steel (MR/T041544/1). The Spanish National Centre for Electron Microscopy at the Complutense University in Madrid and the X-ray diffraction laboratory at CENIM-CSIC are acknowledged for the use of their experimental facilities.

Appendix A. Supplementary data

Supplementary material related to this article can be found online at https://doi.org/10.1016/j.actamat.2024.120018.

References

[1] M.B. Balajaddeh, H. Naffakh-Moosavy, Pulsed Nd: YAG laser welding of 17-4 PH stainless steel: Microstructure, mechanical properties, and weldability investigation, Opt. Laser Technol. 119 (2019) 105651.

[2] M. Niu, K. Yang, J. Luan, W. Wang, Z. Jiao, Cu-assisted austenite reversion and enhanced TRIP effect in maraging stainless steels, J. Mater. Sci. Technol. 104 (2022) 52–58.

[3] J. Onoro, Martensite microstructure of 9–12% Cr steels weld metals, J. Mater. Process. Technol. 180 (1–3) (2006) 137–142.

[4] X. Nong, X. Zhou, J. Li, Y. Wang, Y. Zhao, M. Brochu, Selective laser melting and heat treatment of precipitation hardening stainless steel with a refined microstructure and excellent mechanical properties, Scr. Mater. 178 (2020) 7–12.

[5] M. Murayama, K. Hono, Y. Katayama, Microstructural evolution in a 17-4 PH stainless steel after aging at 400°C, Metall. Mater. Trans. A. 30 (1999) 345–353.

[6] E.V. Pereloma, A. Shekhter, M.K. Miller, S.P. Ringer, Ageing behaviour of an Fe–20Ni–1.8 Mn–1.6 Ti–0.59 Al (wt%) maraging alloy: Clustering, precipitation and hardening, Acta Mater. 52 (19) (2004) 5589–5602.

[7] K.-S. Kim, J.-H. Kang, S.-J. Kim, Effects of carbon and nitrogen on precipitation and tensile behavior in 15Cr-15Mn-4Ni austenitic stainless steels, Mater. Sci. Eng. A. 712 (2018) 114–121.

[8] N. Haghdadi, M. Laleh, M. Moyle, S. Primig, Additive manufacturing of steels: A review of achievements and challenges, J. Mater. Sci. 56 (2021) 64–107.

[9] H. Ramadas, A.K. Nath, S. Sarkar, P. Ganesh, R. Kaul, J.D. Majumdar, Fatigue crack growth rate and fracture toughness evaluation of 15-5 precipitation hardening stainless steel fabricated by laser powder bed fusion process, Mater. Sci. Eng. A. 861 (2022) 144356.

[10] S. Sabooni, A. Chabok, S. Feng, H. Blaauw, T. Pijper, H. Yang, Y. Pei, Laser powder bed fusion of 17–4 PH stainless steel: A comparative study on the effect of heat treatment on the microstructure evolution and mechanical properties, Addit. Manuf. 46 (2021) 102176.

[11] M. Moyle, N. Haghdadi, W. Davids, X. Liao, S. Ringer, S. Primig, Evidence of in-situ Cu clustering as a function of laser power during laser powder bed fusion of 17–4 PH stainless steel, Scr. Mater. 219 (2022) 114896.

[12] L.K. Unti, L. Aota, A. Jardini, A.P. Tschiptschin, H.R.Z. Sandim, E. Jägle, K.D. Zilnyk, Microstructural characterization of 15-5 PH stainless steel processed by laser powder-bed fusion, Mater. Charact. 181 (2021) 111485.

[13] S.R. Narasimharaju, W. Zeng, T.L. See, Z. Zhu, P. Scott, X. Jiang, S. Lou, A comprehensive review on laser powder bed fusion of steels: Processing, microstructure, defects and control methods, mechanical properties, current challenges and future trends, J. Manuf. Process. 75 (2022) 375–414.

[14] M.P. Haines, M.S. Moyle, V.V. Rielli, V. Luzin, N. Haghdadi, S. Primig, Experimental and computational analysis of site-specific formation of phases in laser powder bed fusion 17–4 precipitate hardened stainless steel, Addit. Manuf. 73 (2023) 103686.

[15] S. Vunnam, A. Saboo, C. Sudbrack, T.L. Starr, Effect of powder chemical composition on the as-built microstructure of 17-4 PH stainless steel processed by selective laser melting, Addit. Manuf. 30 (2019) 100876.

[16] D. Zhao, Y. Guo, R. Lai, Y. Wen, P. Wang, C. Liu, Z. Chen, C. Yang, S. Li, W. Chen, et al., Abnormal three-stage plastic deformation in a 17-4 PH stainless steel fabricated by laser powder bed fusion, Mater. Sci. Eng. A. 858 (2022) 144160.

[17] L.-L. Zhang, Y. Zhou, X. Yang, Y.-K. Wei, J.-Y. Wang, S.-F. Liu, Y. Wang, Effect of heat input on the microstructure and mechanical properties of the deposition obtained by selective laser melting (SLM) of precipitation hardened martensitic stainless steel, Mater. Charact. (2023) 113093.

[18] T. Zhou, T. Zheng, A.B. Yildiz, G. Spartacus, M. Rolinska, R. Cubitt, P. Hedström, Microstructure control during deposition and post-treatment to optimize mechanical properties of wire-arc additively manufactured 17-4 PH stainless steel, Addit. Manuf. 58 (2022) 103047.

[19] B. Lv, F. Wang, X. Niu, L. Zhang, X. Wu, Y. Lai, B. Hong, S. Cao, In-situ formed graded microstructure and mechanical property of selective laser melted 15–5 PH stainless steel, Mater. Sci. Eng. A. 847 (2022) 143340.

[20] T. Muslim, T. Karagoz, S. Kurama, P. Sezer, O.F. Yazici, R. Ozkok, Laser metal deposition of 17–4 PH stainless steel: Geometrical, microstructural, and mechanical properties investigation for structural applications, CIRP J. Manuf. Sci. Technol. 41 (2023) 69–79.

[21] P. Nezhadfar, R. Shrestha, N. Phan, N. Shamsaei, Fatigue behavior of additively manufactured 17-4 PH stainless steel: Synergistic effects of surface roughness and heat treatment, Int. J. Fatigue 124 (2019) 188–204.

[22] Z. Wang, H. Li, Q. Shen, W. Liu, Z. Wang, Nano-precipitates evolution and their effects on mechanical properties of 17-4 precipitation-hardening stainless steel, Acta Mater. 156 (2018) 158–171.

[23] X. Nong, X. Zhou, Effect of scanning strategy on the microstructure, texture, and mechanical properties of 15-5 PH stainless steel processed by selective laser melting, Mater. Charact. 174 (2021) 111012.

[24] X. Nong, X. Zhou, Y. Wang, L. Yu, J. Li, Effects of geometry, location, and direction on microstructure and mechanical properties of 15–5 PH stainless steel fabricated by directed energy deposition, Mater. Sci. Eng. A. 821 (2021) 141587.

[25] J.-R. Lee, M.-S. Lee, H. Chae, S.Y. Lee, T. Na, W.-S. Kim, T.-S. Jun, Effects of building direction and heat treatment on the local mechanical properties of direct metal laser sintered 15-5 PH stainless steel, Mater. Charact. 167 (2020) 110468.

[26] S. Sarkar, S. Mukherjee, C.S. Kumar, A.K. Nath, Effects of heat treatment on microstructure, mechanical and corrosion properties of 15-5 PH stainless steel parts built by selective laser melting process, J. Manuf. Process. 50 (2020) 279–294.

[27] S. Sarkar, C.S. Kumar, A.K. Nath, Effects of heat treatment and build orientations on the fatigue life of selective laser melted 15-5 PH stainless steel, Mater. Sci. Eng. A. 755 (2019) 235–245.

[28] B. Zhang, H. Wang, X. Ran, X. Nie, J. Wang, B. He, Microstructure and mechanical properties of high-efficiency laser-directed energy deposited 15-5 PH stainless steel, Mater. Charact. 190 (2022) 112080.

[29] A. Ščetinec, D. Klobčar, A. Nagode, T. Vuherer, D. Bračun, U. Trdan, Optimisation of precipitation hardening for 15-5 PH martensitic stainless steel produced by wire arc directed energy deposition, Sci. Technol. Weld. Join. (2023) 1–11.

[30] I. Avula, A.C. Arohi, C.S. Kumar, I. Sen, Microstructure, corrosion and mechanical behavior of 15-5 PH stainless steel processed by direct metal laser sintering, J. Mater. Eng. Perform. 30 (9) (2021) 6924–6937.

[31] H. Chae, M.Y. Luo, E.-W. Huang, E. Shin, C. Do, S.-K. Hong, W. Woo, S.Y. Lee, Unearthing principal strengthening factors tuning the additive manufactured 15-5 PH stainless steel, Mater. Charact. 184 (2022) 111645.

[32] M. Abdelshehid, K. Mahmodieh, K. Mori, L. Chen, P. Stoyanov, D. Davlantes, J. Foyos, J. Ogren, R. Clark Jr., O. Es-Said, On the correlation between fracture toughness and precipitation hardening heat treatments in 15-5 PH stainless steel, Eng. Fail. Anal. 14 (4) (2007) 626–631.

[33] M. Srinivas, L.M. Patnaik, Genetic algorithms: A survey, Computer 27 (6) (1994) 17–26.

[34] J.-O. Andersson, T. Helander, L. Höglund, P. Shi, B. Sundman, Thermo-Calc & DICTRA, computational tools for materials science, CALPHAD 26 (2) (2002) 273–312.

[35] H. Eskandari Sabzi, S. Maeng, X. Liang, M. Simonelli, N.T. Aboulkhair, P.E. Rivera-Díaz-del Castillo, Controlling crack formation and porosity in laser powder bed fusion: Alloy design and process optimisation, Addit. Manuf. 34 (2020) 101360.

[36] K. Li, J. Zhan, T. Yang, A.C. To, S. Tan, Q. Tang, H. Cao, L.E. Murr, Homogenization timing effect on microstructure and precipitation strengthening of 17–4PH stainless steel fabricated by laser powder bed fusion, Addit. Manuf. 52 (2022) 102672.

[37] P. Nezhadfar, P.R. Gradl, S. Shao, N. Shamsaei, Microstructure and deformation behavior of additively manufactured 17–4 stainless steel: Laser powder bed fusion vs. laser powder directed energy deposition, JOM (2022) 1–13.

[38] R.M. Sebdani, H. Bilan, J. Gale, J. Wanni, G. Madireddy, M. Sealy, A. Achuthan, Ultrasonic impact treatment (UIT) combined with powder bed fusion (PBF) process for precipitation hardened martensitic steels, Addit. Manuf. 84 (2024) 104078.

[39] S.-M. Yeon, J. Yoon, T.B. Kim, S.H. Lee, T.-S. Jun, Y. Son, K. Choi, Normalizing effect of heat treatment processing on 17-4 PH stainless steel manufactured by powder bed fusion, Metals 12 (5) (2022) 704.

[40] C. Li, Y. Chen, X. Zhang, T. Liu, Y. Peng, K. Wang, Effect of heat treatment on microstructure and mechanical properties of 17-4PH stainless steel manufactured by laser-powder bed fusion, J. Mater. Res. Technol. 26 (2023) 5707–5715.

[41] H. Eisazadeh, S. Khadka, X. Wang, P. Yuya, A comparative study of the mechanical characteristics of additively and conventionally fabricated 17-4 precipitation hardened stainless steel, Prog. Addit. Manuf. (2024) 1–19.

[42] M. Moyle, N. Haghdadi, F. Theska, M. Haines, X. Liao, S. Ringer, S. Primig, Effect of compositional variations on the heat treatment response in 17-4 PH stainless steel fabricated by laser powder bed fusion, Mater. Charact. (2024) 113768.

[43] C. Garcia-Cabezon, M. Castro-Sastre, A.I. Fernandez-Abia, M.L. Rodriguez-Mendez, F. Martin-Pedrosa, Microstructure–hardness–corrosion performance of 17–4 precipitation hardening stainless steels processed by selective laser melting in comparison with commercial alloy, Met. Mater. Int. 28 (11) (2022) 2652–2667.

[44] M.P. Haines, M.S. Moyle, V.V. Rielli, N. Haghdadi, S. Primig, Site-specific Cu clustering and precipitation in laser powder-bed fusion 17–4 PH stainless steel, Scr. Mater. 241 (2024) 115891.

[45] S. An, D.-R. Eo, I. Sohn, K. Choi, Homogenization on solution treatment and its effects on the precipitation-hardening of selective laser melted 17-4PH stainless steel, J. Mater. Sci. Technol. 166 (2023) 47–57.

[46] K. Ishida, Calculation of the effect of alloying elements on the Ms temperature in steels, J. Alloys Compd. 220 (1–2) (1995) 126–131.

[47] W. Xu, P. Rivera-Díaz-del Castillo, W. Yan, K. Yang, D. San Martín, L. Kestens, S. Van Der Zwaag, A new ultrahigh-strength stainless steel strengthened by various coexisting nanoprecipitates, Acta Mater. 58 (11) (2010) 4067–4075.

[48] T. Ungár, A. Borbély, The effect of dislocation contrast on X-ray line broadening: A new approach to line profile analysis, Appl. Phys. Lett. 69 (21) (1996) 3173–3175.

[49] K. Thompson, D. Lawrence, D. Larson, J. Olson, T. Kelly, B. Gorman, In situ site-specific specimen preparation for atom probe tomography, Ultramicroscopy 107 (2–3) (2007) 131–139.

[50] P. Karimi, E. Sadeghi, J. Ålgårdh, A. Keshavarzkermani, R. Esmaeilizadeh, E. Toyserkani, J. Andersson, Columnar-to-equiaxed grain transition in powder bed fusion via mimicking casting solidification and promoting in situ recrystallization, Addit. Manuf. 46 (2021) 102086.

[51] J. Xu, Y. Ding, Y. Gao, H. Wang, Y. Hu, D. Zhang, Grain refinement and crack inhibition of hard-to-weld inconel 738 alloy by altering the scanning strategy during selective laser melting, Mater. Des. 209 (2021) 109940.

[52] H. Eskandari Sabzi, N.T. Aboulkhair, X. Liang, X.-H. Li, M. Simonelli, H. Fu, P.E. Rivera-Diaz-del Castillo, Grain refinement in laser powder bed fusion: The influence of dynamic recrystallization and recovery, Mater. Des. 196 (2020) 109181.

[53] A.C.d.F. Silveira, R. Fechte-Heinen, J. Epp, Microstructure evolution during laser-directed energy deposition of tool steel by in situ synchrotron X-ray diffraction, Addit. Manuf. 63 (2023) 103408.
[54] H. Zhang, H. Xiao, X. Fang, Q. Zhang, R. Logé, K. Huang, A critical assessment of experimental investigation of dynamic recrystallization of metallic materials, Mater. Des. 193 (2020) 108873.
[55] T. Nyyssönen, P. Peura, V.-T. Kuokkala, Crystallography, morphology, and martensite transformation of prior austenite in intercritically annealed high-aluminum steel, Metall. Mater. Trans. A. 49 (2018) 6426–6441.
[56] D. Ludwigson, A. Hall, The Physical Metallurgy of Precipitation-Hardenable Stainless Steels, vol. 111, Defense Metals Information Center, Battelle Memorial Institute, 1959.
[57] M. Shirdel, H. Mirzadeh, M. Parsa, Nano/ultrafine grained austenitic stainless steel through the formation and reversion of deformation-induced martensite: Mechanisms, microstructures, mechanical properties, and TRIP effect, Mater. Charact. 103 (2015) 150–161.
[58] T. Lienert, J. Lippold, Improved weldability diagram for pulsed laser welded austenitic stainless steels, Sci. Technol. Weld. Join. 8 (1) (2003) 1–9.
[59] M. Moyle, N. Haghdadi, X. Liao, S. Ringer, S. Primig, On the microstructure and texture evolution in 17-4 PH stainless steel during laser powder bed fusion: Towards textural design, J. Mater. Sci. Technol. 117 (2022) 183–195.
[60] J. Radhakrishnan, P. Kumar, S.S. Gan, A. Bryl, J. McKinnell, U. Ramamurty, Microstructure and tensile properties of binder jet printed 17–4 precipitation hardened martensitic stainless steel, Mater. Sci. Eng. A. 860 (2022) 144270.
[61] H.J. Im, K. Ryou, T.H. Kang, S. Jimbo, S. Nambu, J. Han, P.-P. Choi, Thermally driven changes in the microstructure and mechanical properties of martensitic 15–5 precipitation-hardened stainless steel during directed energy deposition, Addit. Manuf. 74 (2023) 103729.
[62] E. Kuramoto, Y. Aono, K. Kitajima, Thermally activated slip deformation of high purity iron single crystals between 4.2 K and 300 K, Scr. Metall. 13 (11) (1979) 1039–1042.
[63] H. Sieurin, J. Zander, R. Sandström, Modelling solid solution hardening in stainless steels, Mater. Sci. Eng. A. 415 (1–2) (2006) 66–71.
[64] T. Simm, L. Sun, S. McAdam, P. Hill, M. Rawson, K. Perkins, The influence of lath, block and prior austenite grain (PAG) size on the tensile, creep and fatigue properties of novel maraging steel, Materials 10 (7) (2017) 730.
[65] B. Kim, E. Boucard, T. Sourmail, D. San Martín, N. Gey, P.E.J. Rivera-Díaz-del Castillo, The influence of silicon in tempered martensite: Understanding the microstructure–properties relationship in 0.5–0.6 wt.% C steels, Acta Mater. 68 (2014) 169–178.
[66] G. Yeli, M.A. Auger, K. Wilford, G.D. Smith, P.A. Bagot, M.P. Moody, Sequential nucleation of phases in a 17-4 PH steel: Microstructural characterisation and mechanical properties, Acta Mater. 125 (2017) 38–49.
[67] Q. Guo, M. Qu, C.A. Chuang, L. Xiong, A. Nabaa, Z.A. Young, Y. Ren, P. Kenesei, F. Zhang, L. Chen, Phase transformation dynamics guided alloy development for additive manufacturing, Addit. Manuf. 59 (2022) 103068.
[68] Y. Lin, D.-X. Wen, M.-S. Chen, X.-M. Chen, A novel unified dislocation density-based model for hot deformation behavior of a nickel-based superalloy under dynamic recrystallization conditions, Appl. Phys. A. 122 (2016) 1–16.
[69] D. Saha, E. Biro, A. Gerlich, Y. Zhou, Martensite tempering kinetics: Effects of dislocation density and heating rates, Mater. Charact. 168 (2020) 110564.
[70] M. Natori, Y. Futamura, T. Tsuchiyama, S. Takaki, Difference in recrystallization behavior between lath martensite and deformed ferrite in ultralow carbon steel, Scr. Mater. 53 (5) (2005) 603–608.
[71] R. Song, D. Ponge, D. Raabe, J. Speer, D. Matlock, Overview of processing, microstructure and mechanical properties of ultrafine grained bcc steels, Mater. Sci. Eng. A. 441 (1–2) (2006) 1–17.
[72] E. Galindo-Nava, P. Rivera-Díaz-del Castillo, Modelling plastic deformation in BCC metals: Dynamic recovery and cell formation effects, Mater. Sci. Eng. A. 558 (2012) 641–648.
[73] R. Kapoor, G.B. Reddy, A. Sarkar, Discontinuous dynamic recrystallization in α-Zr, Mater. Sci. Eng. A. 718 (2018) 104–110.